INTERNATIONAL JOURNAL of RENEWABLE ENERGY RESEARCH
S. Xu and G. Yang, Vol.16, No.2, June, 2026

Wind Energy Utilization in Coastal Environmental Design: Challenges and Innovations in Balancing Ecology and Aesthetics

Shilong Xu*‡, Guangyu Yang**

*School of Art and Design, Kaili University, Kaili City, Guizhou Province, 556011, China

**School of Art, Dezhou University, Dezhou City, Shandong Province, 253023, China

(xushilong94@163.com, yangguangyu1973@126.com)

‡ Corresponding Author; Shilong XU, shilongxu11@gmail.com

Received: 05.02.2026 Accepted:15.04.2026

Abstract- In coastal landscape design, the arrangement of small-scale wind turbines often generates environmental integration challenges, including ecological disturbance, spatial fragmentation, and visual conflict. This paper proposes a collaborative optimization framework that integrates multi-source sensing data with generative design to balance renewable energy performance and coastal landscape quality. The reported results are derived from a hybrid approach combining field measurements, computational fluid dynamics simulations, and virtual reality-based participant evaluations. By combining dynamic ecological simulation with a closed-loop mechanism of public aesthetic feedback, the framework aims to achieve functional symbiosis and visual harmony between wind energy facilities and sensitive coastal environments. In implementation, a dynamic three-dimensional ecological sensitivity field is constructed by fusing satellite remote sensing, UAV surveys, ecological monitoring data, and bird radar observations, forming rigid ecological constraints for design generation. Morphological parameters, including turbine type, hub height, spacing, and tilt angle, are iteratively adjusted based on performance feedback from computational fluid dynamics wind field simulations. Public aesthetic evaluations collected through immersive virtual reality scenarios are quantified and transformed into computable weights, embedded into an iterative generative design loop to guide form and layout evolution. Through multi-objective optimization, the proposed method refines design solutions that reduce ecological disturbance, maintain stable energy output, and enhance visual compatibility. Ecological, energy, and aesthetic assessments confirm the effectiveness of the proposed method, with detailed metric ranges provided in the results section.

Keywords Coastal wind energy, ecological design, data fusion, generative optimization, VR evaluation.

1. Introduction

Coastlines, as the surfaces at which energy flux converges with ecological processes, are being opened as reserve spaces for energy capture in the form of renewable [1], [2]. The production of small wind turbines in the coastal region is not only a technical activity of harvesting energy, but also a dynamic systems coalescence, such as flows of air, migration of biological organisms, and visual perception [3]. Their design should be informed by the changing environmental backdrops and the underlying order (or aesthetic structure) of the dynamic [4], [5], [6]. Under the dual focus on carbon-neutral targets and ecosystem resilience stipulations, the coastal spatial weaving presents a challenging enabling environment for the wind energy infrastructure to harmoniously meld with the low-impact-high-integrity coastal domain to realize the synergy of technical-natural systems [7], [8]. In this transition, the design medium adopts a new role by modulating the relationship between people, technology, and coastal environments. Scientific modeling and cross-scale integration are used to position infrastructures as interfaces connecting energy cycles and landscape narratives.

At present, the spatial coordination of coastal wind power plants suffers from a three-way disconnection: slow

response of landscape ecology, performance simulation of stasis, and aesthetic evaluation of subjectivity. The identification of ecologically sensitive areas has traditionally relied on static layer stacking, which makes it problematic to account for spatiotemporal variations in tidal rhythms, vegetation succession, and routes of migrating birds, resulting in a lack of dynamism and adaptability in land-use constraints [9], [10]. The performance of wind turbines is commonly evaluated on the basis of an idealized wind field, leaving out the effect of terrain disruptions and diurnal sea-land breezes on the formation of local winds. More importantly, sensitivity to the visual impact of facilities is strongly context-specific among the public [11], [12]; current testing frequently involves questionnaires or ratings of static images, replicating the environmental context, and sometimes cognition conflicts are encountered by participants after implementation of design outcomes [13], [14]. In addition, the process of making design decisions is separated from the environmental feedback loop in terms of the parameters of technique, and there is no quantitative relationship between the shape generation process and the expression of ecology and anticipation of visuals [15], [16]. This divergence makes the trajectory of optimization converge on the pursuit of single-objective extremes, which is not beneficial to the convergence of collaborative multi-objective [17], [18]. Abstracting wind turbines to purely geometric footprints strips their formal conversation with dune contours, site lines to the sea, and vegetation skylines of any design basis [19], [20]. The real challenge lies in constructing an integrated framework that can simultaneously analyze ecological dynamics, aerodynamic performance, and perceptual preferences, and transform them into actionable design variables, so that wind energy facilities neither sacrifice functional efficiency nor diminish the intrinsic value of the landscape.

Existing research on the integration of wind energy facilities with the environment focuses on constraint modeling, performance simulation, and visual evaluation. Some studies have attempted to integrate ecological data through geographic information systems to establish suitability zoning models to guide facilities to avoid sensitive areas. However, such methods are mostly based on fixed-weight superposition analysis and do not fully consider the temporal heterogeneity and spatial nonlinear response of ecological factors [21], [22]. Another type of work focuses on microscale wind field numerical simulation, using computational fluid dynamics to predict the output power of wind turbines under different terrain conditions to support layout optimization. However, such simulations are usually detached from ecological and visual dimensions, forming an independent technical closed loop [23], [24]. At the aesthetic level, some studies have introduced a landscape visual impact assessment system. Darabi S applied a multi-standard decision-making method, combined with receptor sensitivity factors, to assess the visual impact of the Mangil wind farm on the urban environment and tourism landscape of Gilan Province, Iran. It was found that important viewpoints, such as tourist destinations and buildings, were highly visually impacted, and the technology used verified the reliability of the method at 84.73% similarity [25]. Although some attempts have been made to apply multi-objective optimization algorithms to wind power layout, their objective functions are still limited to power generation and cost, and ecological and aesthetic indicators are often simplified to penalty terms or threshold restrictions, failing to achieve deep integration with morphological generation [26], [27], [28]. Overall, existing research has obvious gaps in cross-scale data fusion, multi-dimensional objective quantification, and the construction of design iteration closed loops, and has not yet formed a collaborative design paradigm that can connect environmental perception, performance-driven, and perception feedback. In recent years, the cross-application of multi-source perception and generative design has provided new ideas for infrastructure layout in complex environmental systems. Remote sensing images and UAV aerial surveys have been used for high-precision terrain and vegetation mapping, supporting dynamic environmental monitoring [29]; radar and acoustic sensors have enabled continuous tracking of the activity patterns of flying animals, enhancing the real-time nature of ecological response [30]. Based on this, some studies have attempted to use CFD simulation results as input parameters to drive parametric models to adjust wind turbine layout and tower shape, and initially realize performance-oriented shape generation, which has been used for wind power prediction and dynamic sensing technology [31], [32]. Dong X proposed a new conditional latent diffusion model to generate short-term wind power scenarios. By decomposing the task into deterministic prediction and prediction error generation, it significantly improved generation performance and denoising efficiency, showing significant advantages compared with existing methods [33]. Further research has constructed an optimization process based on a proxy model, replacing the time-consuming physical process of simulation with a fast-response mathematical approximation, thereby improving iteration efficiency [34]. Martinez-Neri I F explored the applicability of the supply chain integration dimension in the project manufacturing environment (taking offshore wind farm construction as an example) through case analysis. It found that some dimensions are similar to large-scale manufacturing environments, but dimensions such as relationship management, information integration, and sharing are unique in large-scale projects. It also emphasized the necessity of formal contracts and confidentiality agreements in resource-intensive projects [35]. However, these methods still fall short in terms of integration depth: ecological data is mostly used as background conditions and does not directly participate in the morphological generation logic. CFD simulation cycles are long, making it difficult to embed them into high-frequency iterative processes; public perception data collection still relies on discrete samples and lacks a linkage mechanism with virtual reality immersive environments. And more critically, the nonhomogeneous computational structure of the modules causes distortion in the transmission of information and feedback delay. In this paper, it is proposed to convert multi-source sensing data streams into dynamic ecological fields, to integrate a lightweight wind field proxy model with a VR-based aesthetic feedback loop, and to embed this in a generative design system to create a full-chain co-design framework of "perception-simulation-generation-feedback," breaking through the constraints of existing approaches in timeliness, coupling, and user experience integration.

The objective of this paper is to develop a collaborative design methodology for wind energy systems in a coastal region. Contributions: There are three aspects, which are best regarded as the key contributions. Firstly, a dynamic ecological sensitivity field (DESF) is introduced to fuse multi-source time-series data (satellites, drones, and biological monitoring) for dynamic modeling of habitat alterations to provide spatiotemporally responsive design constraints. Secondly, it devises a coupling strategy between a lightweight CFD surrogate model and a generative algorithm, which facilitates control over the turbine type, height, and tilt angle under the wind field performance constraints, and enhances the alignment of morphological generation with aerodynamic performance. Thirdly, it designs and implements a virtual reality-based public aesthetic feedback system, which collects perceptual scores in the course of immersive scene exposure and translates them into computationally visual coordination weights to be integrated into a multi-objective optimization scheme. The novelty of this framework lies in the closed-loop integration of the dynamic ecological sensitivity field, the lightweight CFD surrogate model, and the VR-based aesthetic feedback system into a unified generative design process, whereas the individual techniques draw upon existing methods from ecological modeling, aerodynamic simulation, and virtual reality assessment. The combination of these three developments leads to a closed-loop design methodology in which ecological preservation, energy conservation, and landscape attractiveness can be progressively improved in the synthesis process without being compromised/exchanged off subsequently. Compared to traditional methods, this paper's approach focuses on the deep coupling of data flow and design flow to prevent fragmented processing of different dimensional metrics, and guarantee that the final design solution is optimal from the perspectives of low ecological disturbance, power generation stability, and visual integration. The research results provide not only a practical technical approach for the exploitation of coastal wind energy but also theoretically support and methodologically guide the shift of paradigm in infrastructure projects in ultra-sensitive landscapes.

2. Eco-Aesthetic Collaborative Design Framework for Coastal Wind Energy Facilities

Based on the core modules of coastal wind energy systems, Fig. 1 outlines the proposed integrated design process with a three-level structure. The lower tier is a fusion of three disparate data sources (satellite remote sensing, UAVs, and bird radar) and 3D modeling (CFD simulation and VR perception). The second tier converts raw data into dynamic ecological constraints, performance-based morphological parameters, and numerically computable aesthetic weights. The third layer uses multi-objective generative optimization to obtain a Pareto solution set. After a manager picks the points of interest, the solution is exported to the BIM (Building Information Modeling) platform to be further detailed for implementation design. All are systematically relating with non-processed-oriented thought – data-driven, goal coupling, and closed-loop feedback, so to speak. It shows the synchronous cooperation between ecological response, energy saving, and landscape aesthetics during design generation, meeting the design ideology of deep integration of infrastructure and natural systems in coastal areas.

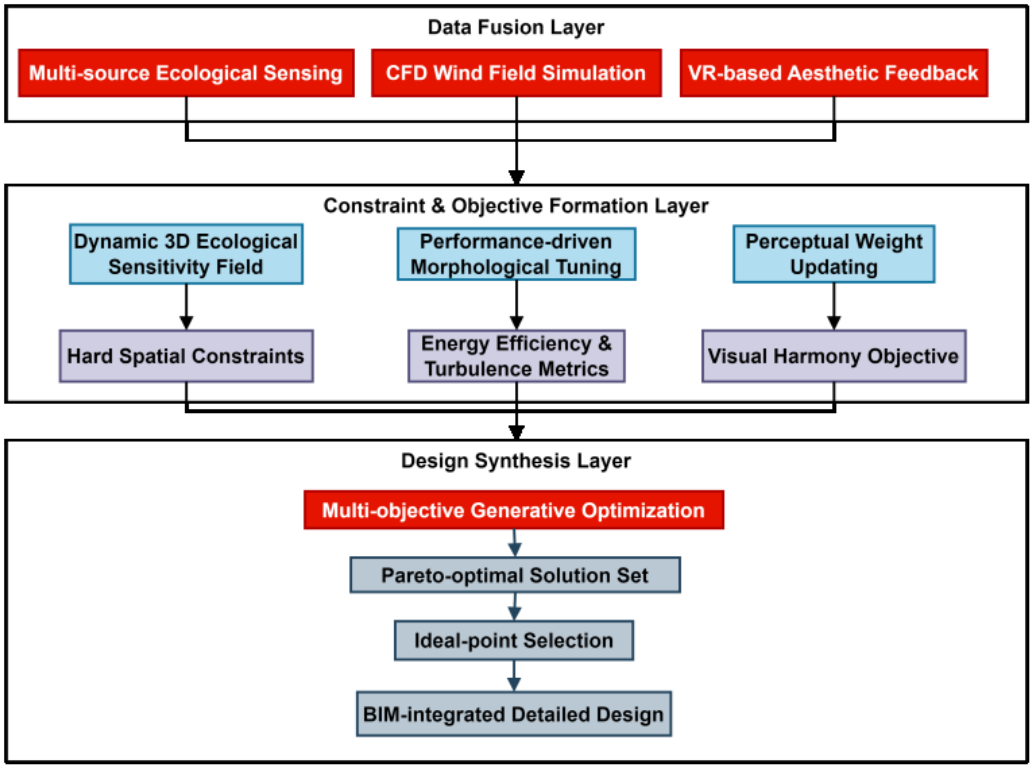

Fig. 1. Integrated design framework for coastal wind energy facilities.

Step 1: Fuse multi-source ecological sensing data from satellites, UAVs, bird radar, and ground stations with CFD wind field simulations and VR-based aesthetic feedback. Step 2: Construct a dynamic three-dimensional ecological sensitivity field, apply performance-driven morphological tuning of turbine parameters, and update perceptual weights from public VR scores. Step 3: Establish hard spatial constraints from the ecological sensitivity field, define energy efficiency and turbulence metrics from CFD simulations, and formulate the visual harmony objective from aesthetic feedback. Step 4: Execute multi-objective generative optimization using NSGA-II to generate a Pareto-optimal solution set balancing ecological disturbance, energy output, and visual integration. Step 5: Select the compromise solution via the ideal-point method and export the chosen design to a BIM platform for detailed implementation.

2.1. Multi-Source Ecological Sensing and Dynamic Constraint Generation

Coastal ecosystem components are highly dynamic and spatially heterogeneous; thus, sensing information of high temporal frequency with fine spatial granularity is needed. Satellite remote sensing offers a consistent view of land cover at regional to global scales over decades using multispectral imagery from, inter alia, the Sentinel-2 mission. UAV aerial photography collects orthophotos with a spatial resolution in centimeters at representative ecological nodes, which are used for extracting the boundaries of vegetation patches as well as the micro-topographic forms of sand dunes. Ecological stations of the ground are installed in representative units of habitat to continuously measure soil moisture, wind speed profiles, and vegetation phenological parameters. Bird radars are placed along migration pathways where they detect the density and direction of low-flying organisms using S-band pulse Doppler technology. The spatiotemporal referencing of the above data sources is different, which requires coordinate system transformation and time window matching. Spatial registration implements bilinear interpolation to resample all rasters to the same reference grid, with the projection system as UTM Zone 51N. Then, in the temporal dimension, uniformly spaced time series are generated, and cubic spline interpolation is adopted to complete missing frames of asynchronous observation data, in order to represent the ecological evolution path continuously.

Semantic consistency modeling at the feature layer is used in multi-source data fusion. The change rate of vegetation cover is derived from the first difference of the Normalized Vegetation Index time series and indicates the rate of progression of plant community growth or degradation. Dune migration vectors are determined by computing the surface displacement fields between digital elevation models (DEMs) at different temporal stages. A nearest-point algorithm is used to iteratively register 3D point clouds for extracting the direction of horizontal movement and the annual average displacement. Bird activity hotspots are created by means of radar point cluster analysis. The DBSCAN (Density-Based Spatial Clustering of Applications with Noise) is run on flight paths to find clusters of paths, and each cluster is given an intensity weight. Several indices are normalized and then mapped onto a 3D geospatial space to result in an evolving ecological response field. It reinforces the nonlinear ecological interactions among ecological variables instead of information distortion due to a simple weighted composite.

Table 1. Sensor platforms used for ecological monitoring with spatial resolution temporal frequency and data output types

Sensor Type	Spatial Resolution	Temporal Frequency	Data Dimension
Sentinel-2	10 m	5 d	2D raster
UAV orthophoto	0.05 m	15 d	2D raster
UAV point cloud	0.1 m	15 d	3D point cloud
Ground monitoring station	Point-based	10 min	Time series vector
Avian radar	1.5° angular res.	1 s	3D trajectory stream
Tide gauge	Point-based	1 min	Time series scalar

Note: UAV stands for Unmanned Aerial Vehicle.

Table 1 presents a concise overview of six types of sensor platforms, detailing their spatial resolution, temporal frequency, payload types, and output data dimensions in coastal ecological sensing. The data span satellite remote sensing and ground-based fixed equipment; modality-specific timescales vary from seconds (radar birds) to half-monthly (UAV point clouds). Together with spatial granularity, this serves as the basis for multi-scale, multi-modal dynamic monitoring, offering a structured input source for the ensuing ecological sensitivity field modeling.

After performing multi-source feature extraction, a three-dimensional ecological sensitivity field with a time dimension is established as the spatial access unit for design intervention. This field selects areas not only of static protection but also rhythmic oscillations and responses to abrupt disturbances of the process. Partial differential equations are proposed to model the propagation and decay of ecological state variables in space, resulting in the following continuous field model:

$$\frac{\partial S(\mathbf{x},t)}{\partial t}=D\nabla^2 S(\mathrm{x},t)-\lambda S(\mathrm{x},t)+R(\mathrm{x},t) \quad (1)$$

$S(\mathrm{x},t)$ represents the ecological sensitivity intensity at the location x at time t; D is the diffusion coefficient, controlling the influence range of sensitive information within the spatially adjacent city; λ represents the attenuation rate,

simulating the memory-weakening effect of natural recovery capacity on historical disturbances; $R(x,t)$ is the external driving term, integrating input signals such as real-time monitored vegetation change rate, dune displacement, and bird activity intensity. Parameter values are calibrated using historical vegetation recovery records and migration density observations to maintain ecological realism. The diffusion coefficient D is set to 0.32 $m^2 \cdot h^{-1}$ and the attenuation rate λ to 0.045 h^{-1}. The diffusion coefficient is calibrated by fitting the spatial propagation rate of vegetation cover following disturbance using historical vegetation recovery records, with a nonlinear least-squares procedure minimizing the root-mean-square error between the model-predicted recovery front positions and remote sensing observations. The attenuation rate is calibrated from the decay curve of migration density with distance from core habitat derived from bird radar observations, using an exponential decay model. The weights in the external driving term R(x,t) are 0.4 for the vegetation change rate, 0.3 for dune displacement, and 0.3 for bird activity intensity; these weights are determined by principal component analysis of the three normalized time series, taking the loading coefficients of the first principal component. All parameter calibrations are validated against a two-year historical dataset independent of the training data from the study area, ensuring a spatial agreement above 85% between the simulated ecological sensitivity field and the measured distribution of sensitive points. This equation is solved numerically using the finite difference method, updating the entire field value hourly on a regular grid to generate a dynamically evolving sensitivity distribution.

From the quantization threshold of the sensitivity field, the spatial control level can be derived. Sensitivity intensities that fall within the top 10% are designated as non-disturbance areas, where no infrastructure can be built, so that core habitats are not disturbed. The area between the 70th and 90th percentiles is established as a flexible buffer zone where facility deployments can be established temporarily under specific seasonal conditions, though with ecological compensation. The rest of the domain is considered the controllable zone, which is where the number of wind turbines must be placed. Spatial intersections are determined by applying a contour surface extraction algorithm (Marching Cubes) to obtain a smooth, closed 3D geometric object that can be directly imported into the following design process as a hard constraint.

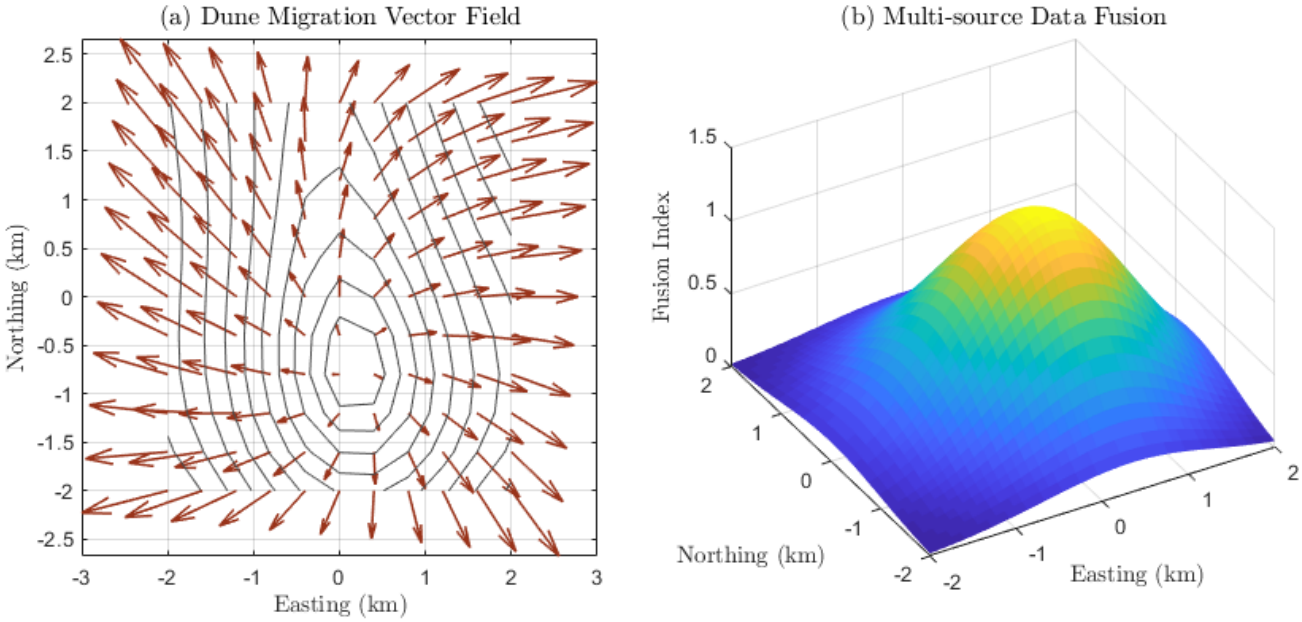

Fig. 2. The spatial coupling analysis of dune migration and multi-source data fusion.

Fig. 2a shows the vector field of dune migration, and it indicates the spatial variability of the coastal dynamic system. The arrows represent the modulation of sediment transport trajectories by the dominant wind field and tidal influence, and the variation in the length of the vector represents how topography influences the redistribution of airflow. Typical vortex structures appearing in the velocity contours indicate local flow field separation and attachment in the flow field. This spatial pattern is coupled with the distribution of vegetation patches. Fig. 2b displays the multi-source data fusion surface to construct a spatial gradient model of ecological sensitivity. The unimodal shape lies in the geometric center of the map and represents the ecological radiation effect of the core habitat. This is a curved-edge transition that models a gradual loss of ecological value from the core area to the peripheral buffer ring, as opposed to a sudden cutoff. Such a radial representation serves as a sequential decision-making framework for the placement of facilities that circumvents the inflexibility of zonal approaches traditionally used. Together, these two views illustrate the temporally variable physical processes of the coastal ecosystem: the vector field portrays the instantaneous state of physical processes, while the fused surface represents ecological memory at various spatiotemporal scales. This dual representation enables a complete-cycle evaluation from short-term perturbations to long-term cumulative impact for the assessment of site selection for wind energy facilities.

2.2. Aerodynamic Performance-Guided Morphology Generation and Adaptation

2.2.1. High-fidelity wind field simulation and performance response modeling

The coastal landform is complex with extensive airflow acceleration, separation, and reattachment phenomena at the sea-land boundary, all of which influence the local wind environment. The microscale wind field model uses computational fluid dynamics methods to solve a system of incompressible Reynolds-averaged Navier–Stokes equations, along with a k-ε turbulence closed-loop model to represent the flow structure. The computational domain encompasses an area with a radius of two kilometers, with the disturbance implemented through a realistic digital terrain model and surface roughness distribution. The mesh system uses unstructured tetrahedral elements with boundary layer refinement in the region near the turbine. The first layer mesh height is 0.5 meters to ensure the y+ value falls within the valid validation range. The inlet boundary condition is a logarithmic wind speed profile using on-site meteorological tower measurements for comparison, where the outlet is defined by a free outflow boundary condition. The sidewalls and the top surface are slip boundary conditions. The steady-state solver performs iterative calculations until the residuals converge to the order of 1×10^{-5}, obtaining the overall velocity vector and turbulent kinetic energy distribution. The computational mesh contains approximately 2.8 million unstructured tetrahedral cells with a near-wall refinement thickness of 0.5 m, and the steady-state solution converges within 1200 iterations under an under-relaxation factor of 0.3 for pressure and 0.4 for momentum. Mesh independence is confirmed by comparing solutions on 1.9 million, 2.8 million, and 3.6 million cells, with the variation in annual power generation below 1.2% between the two finer meshes. The radial basis function surrogate model achieves a coefficient of determination of 0.94 and a mean absolute error of 3.7% against CFD validation samples.

The coastal wind field is decomposed into its principal components to characterize how each affects turbine performance. Mean wind speed at hub height, derived from the logarithmic boundary-layer profile, determines the baseline power yield. Wind shear, quantified as the exponent of the power-law velocity profile between 10 m and hub height, governs the vertical gradient that increases with tower height. Turbulence intensity, calculated as the ratio of the wind speed standard deviation to the mean over 10-minute intervals from meteorological tower records, introduces load fluctuations and reduces effective energy capture relative to the Betz-limit prediction. Wind gust influence is evaluated using hourly wind variance derived from the same meteorological tower measurements to examine layout stability under fluctuating wind conditions; the gust response index reported in Table 2 represents the ratio of peak instantaneous wind speed deviation to mean speed, averaged across the annual record. Sea-land breeze cycles, with a diurnal period of approximately 12 hours and a measured velocity reversal amplitude of 1.8–3.2 m/s at the study site, impose time-varying inlet boundary conditions that shift the dominant inflow direction between onshore and offshore sectors, thereby altering wake alignment and downstream attenuation. Wake-induced wind speed deficits, computed at sampling planes located two rotor diameters downstream of each turbine, are included as a secondary aerodynamic objective to constrain inter-turbine interference. All six components are incorporated simultaneously into the CFD boundary conditions and the surrogate model input vector to ensure the performance response surfaces reflect the full spectrum of coastal aerodynamic variability.

The performance response surfaces of each wind turbine located at different geographical locations are constructed using simulation results. For each turbine's coordinate, the incoming flow direction, wind speed gradient, and turbulence intensity are extracted as input state variables. These are later fused to the turbine's power curve and start-up/cut-off wind speed thresholds to determine the theoretical annual energy generation. The temporal integration model uses a weighting factor modeling the annual characteristics of wind resource variability at hourly or less frequency and averaged over typically generated annual experiences or typical meteorological datasets:

$$E=\int_0^T P\left(u(\mathrm{x},t)\right)dt \tag{2}$$

E represents the annual power generation in kilowatt-hours; $P\left(u(\mathrm{x},t)\right)$ represents the instantaneous output power of the wind turbine at the location x and time t, mapped from wind speed u to the equipment power characteristic function; T represents the time period of a year. This integration occurs through an accumulation of discrete time steps with a sampling frequency of a unit time interval, not less than 1 hour or more than 1 hour, with a typical meteorological dataset's temporal or yearly reporting structure that covers every hour. At the same time, the kinetic energy dissipation and vortex generation density in the wind turbine wake region are measured to avoid negative impacts on the downstream wind flow, and to use as an additional dual objective evaluation.

2.2.2. Efficient optimization of morphological parameters

Based on a Surrogate Model, adjusting the morphological parameters of the wind turbine requires striking a balance between energy capture efficiency and the local influence of airflows in the environment, through the coordinated configuration of type choice, tower vertical extension length, and the angle of the blades. A discrete design selection library is created for types of units, for both vertical and horizontal axis units, and selected according to start-up wind speed, rated operating conditions, and noise radiation pattern. The tower height variable is increased in 5-meter increments in the 20 to 60-meter height range. At each height level, a CFD mesh system is remapped, and the flow field interaction relationships are updated through local mapping and interpolation. The blade tilt angle is defined as the angle between the plane of rotation and the horizontal plane, adjusted within the range of 0° to 30° to change the windward cross-sectional area and angle of attack distribution, affecting the lift-to-drag ratio and start-up sensitivity.

The morphology adaptation process relies on a surrogate model-driven rapid evaluation mechanism to avoid high-frequency, high-cost simulation calls. A radial basis function neural network is constructed to fit the nonlinear mapping relationship between input parameters and output performance. The training samples are from the previous batch of CFD calculation results, containing no fewer than 200 configuration combinations. Model validation produces a coefficient of determination of 0.94 and a mean absolute error of 3.7 percent against CFD verification samples. The network output includes the predicted annual power generation and the wake extension radius, as components of the optimization objective function.

$$f_1=w_1 \frac{E}{E_{\max}} - w_2 \frac{T}{T_{\max}} \tag{3}$$

f_1 is the overall performance index; T represents the wake influence range; $E_{\max}$ and $T_{\max}$ are the maximum values of the corresponding terms in the sample set, used for normalization; w_1 and w_2 are weighting coefficients, reflecting target preferences. Another sub-objective focuses on the local turbulence enhancement effect:

$$f_2 = \frac{1}{A} \iint_A \left(k'(\mathbf{x})-k_0(\mathbf{x})\right) dA \tag{4}$$

$k'(\mathbf{x})$ represents the increase in turbulent kinetic energy in the area after the wind turbine is installed; $k_0(\mathbf{x})$ is the original background value; A is the affected ground area. This index is used to constrain the degree of airflow fragmentation. The optimization algorithm adopts the Non-dominated Sorting Genetic Algorithm II (NSGA-II), which searches for a design scheme that balances power generation capacity and low disturbance characteristics on the Pareto front, outputs the optimal morphological combination, and locks the parameter configuration.

2.3. Design Iteration Mechanism Embedded with Public Perception Feedback

2.3.1. VR immersive scene construction and real-time perception data acquisition

The public visual acceptance of wind power facilities in coastal landscapes highly depends on the accurate recreation of the spatial context; static images or two-dimensional illustrations are unlikely to trigger a deep cognitive response. A high-fidelity immersive evaluation environment is constructed using virtual reality technology. The 3D model is imported into the Unity engine, and then realistic geographic textures are layered with dynamic lighting models to create interactive scenes. To guarantee the authenticity of the environmental background, topographic elevation, vegetation cover, and sea surface albedo are obtained through the calibration of multi-source remote sensing data. The wind turbine prototypes are designed to actual geometric scale, including tower curvature, blade profile, and material reflectivity. The surface treatment is rendered by a PBR (Physically Based Rendering) process with high fidelity simulation of metallic luster and diffuse reflection. A time-dependent embedding system is enabled, so that users may watch how the space-embedding effect between the facilities along the dune line, at the sea level, and the forest edge changes as the sunlight angle and weather conditions vary.

The participants donned HTC Vive Pro headsets to be immersed in a virtual environment and walked along a pre-planned walking route as viewed from the first-person perspective, with their line of sight locked at 1.6 based on the average adult height. Each trail consisted of five primary viewing nodes, representing common sightline encounters including faraway, side, near, up, and down sightlines. The focus hotspots and trajectories of head rotation are automatically recorded while the participants stayed 90 seconds in each node. A 7-point Likert scale questionnaire emerges after the exposure, asking the participants to evaluate four aspects: “morphological harmony,” “scale appropriateness,” “color integration,” and “dynamic interference” (1=extreme rejection to 7=full acceptance of the presented design), representing their levels of agreement with the corresponding statements. To avoid memory bias, each subject takes three rounds of blind testing with different scenarios. Data acquisition is performed in an anechoic room with the ambient light and background noise controlled to avoid any interference in the feedback signals. Cronbach alpha reliability of the questionnaire reaches 0.89 indicating internal consistency. Test-retest reliability is assessed by re-evaluating the same set of design scenarios with a randomly selected subset of 30 participants two weeks after the initial session, yielding an intraclass correlation coefficient of 0.85 with a 95% confidence interval from 0.79 to 0.90. Inter-rater reliability is calculated using Kendall′s coefficient of concordance, with values of 0.82 for morphological harmony, 0.78 for scale appropriateness, 0.80 for color integration, and 0.76 for dynamic interference, all statistically significant. The standard error of measurement for the rating scale is 0.21 scale points, and the minimum detectable difference is 0.58 scale points, indicating that a change above 0.6 on the 7-point Likert scale represents a true difference in aesthetic preference rather than measurement error. Each trial takes about 25 minutes, and the participants include local residents, tourists, and planning professionals. All participants provide written informed consent prior to engagement in the VR evaluation sessions.

2.3.2. Quantification of aesthetic preferences and mapping of design weights

Following the cleansing, the original rating data is subjected to quantitative analysis, which removes responses with extremely short response times or extreme consistency, and valid samples are kept. A principal component analysis is applied to the four aesthetic dimensions in order to identify dominant perceptual structures. The assessment dimensions are then transformed/reconstructed through the factor loading to become composite indicators with physical interpretation. The individual rating differences are decomposed into fixed and random effects using a mixed-effects model to estimate the influence coefficients of age, length of residence, and professional background on aesthetic judgment, which are subsequently applied to weight and aggregate group

preferences. As a result, a standardized acceptability index for each design attribute is produced, computed as:

$$A_i=\frac{1}{N}\sum_{j=1}^{N} w_j \ s_{ij} \tag{5}$$

A_i denotes the visual acceptance of the i-th design scheme; N is the number of valid participants; s_{ij} is the score of the j-th participant for the scheme; w_j is a weight coefficient, which is obtained through regression analysis on demographic variables and represents the sample's representativeness. This index is injected into the design assessment system as an exogenous input to affect the refabrication of the objective function. The design system optimization weights are not fixed quantities but sequences updated at each iteration. An exponential moving average is used to smooth the score volatility and stabilize the feedback.

$$\alpha_t=\gamma\alpha_{t-1}+(1-\gamma)A_t \tag{6}$$

α_t denotes the visualization coordination weight at the t-th iteration; the current weight value of the previous iteration is denoted by α_{t-1}; A_t is the remaining acceptability index (acceptability index gathered in this iteration); γ is the decay factor (0.7 for t=1, to give higher sensitivity to the new data). This weight influences the objective function of the generation process and controls the rate of the "visual fusion" factor in the multi-objective optimization. After each new scheme is generated, a new round of VR rendering and scoring loop is automatically initiated, completing a closed perception-driven evolution loop. During the generation, the design scheme is gradually converging to the group preference space represented by the continuity of outlines, the rhythm of volume gradient, and the contrast of materials, realizing the implicit embedding of technical facilities in the semantic layer of the landscape.

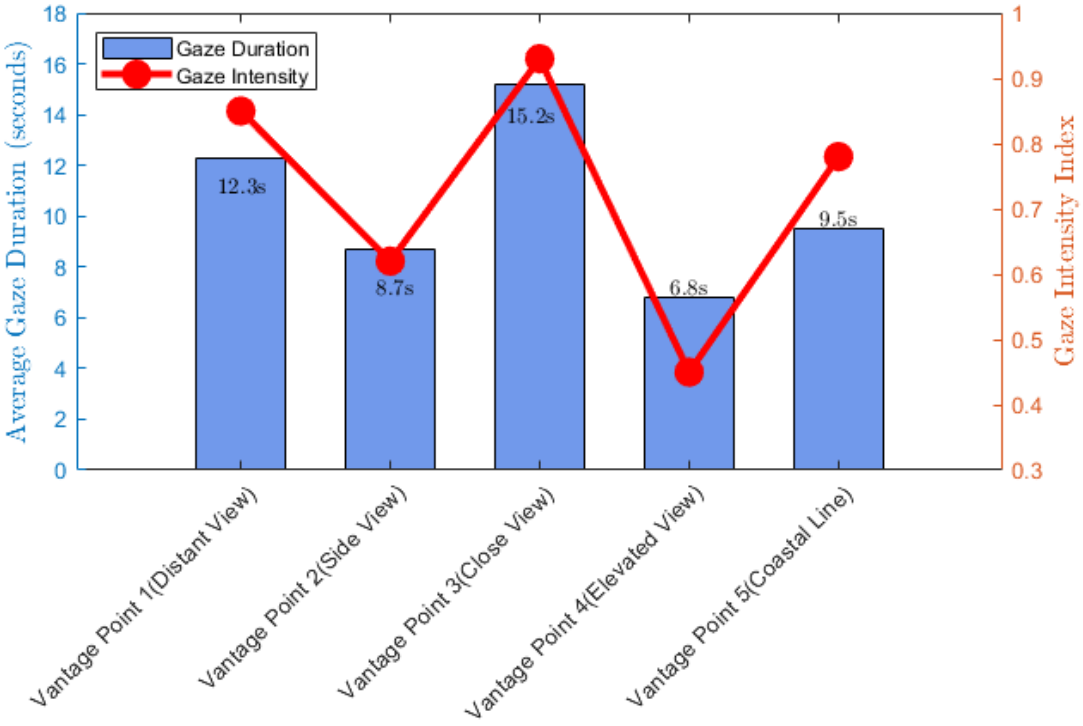

Fig. 3. The distribution of visual attention from different perspectives.

Hotspot distribution of gaze shows that visual cognitive behavior has a tight relation with the feature of viewing space in Fig. 3. The near-field viewing nodes reach the top of the gaze statistics: a mean gaze duration of 15.2 seconds and a gaze intensity index of 0.93. This information indicates the deep processing manner of the human visual system in near-field spatial components. Remote nodes retain a moderate gaze with a gaze duration of 12.3 s and an intensity index of 0.85 that matches the general cognitive properties of the mid-level route. Indeed, top-down nodes have small values for all the measures: secondary status, high-altitude perspective in the landscape sequence, with a gaze duration of 6.8 s, and an intensity index of 0.45, suggesting a relatively small importance value for the high-altitude perspective in the landscape sequence. The positive relationship between gaze duration and intensity index is indicative of directional attentional deployment in the visual modality. The data distribution clearly presents spatial gradients, ranging from near-field depth processing to distant field global perception, which can be regarded as the full visual cognitive map. This difference in spatial cognition provides a quantitative rationale for the importance ranking of landscape nodes, with near-field regions receiving a precedence optimization scale in visual design parameters.

2.4. Generation of Multi-Objective Solutions for Eco-Aesthetic Balance

2.4.1. Multi-objective generative optimization and pareto front solution

The differences in design goals require the development of a unified evaluation system with quantitative and comparable metrics over ecological disturbance, energy output, and visual integration. The constraints and responses from each of the above-mentioned levels are converted into three separate yet interrelated objective functions that are encapsulated in the core of a generative algorithm. The ecological disturbance index is given by the spatial overlap between wind turbine placement and the 3D dynamic sensitivity field. The intrusion quantity is evaluated by the voxel overlap integral method; a smaller one suggests less penetration into the crucial ecological processes. The stability of power generation is represented by annualized equivalent full load hours, which are weighted and aggregated based on the wind resource distribution and unit power characteristic curves, derived from CFD simulation, to represent its energy output under actual operating conditions. Visual integration is the aesthetic acceptability index from the VR feedback system directly, which is added to the objective space as a positive term in the optimization after normalization.

The generative design engine operates on a parametric model, which is subject to the tower height, blade aspect ratio, unit spacing, layout topology, and surface material reflectivity as the design variables, and uses this information to generate a high-dimensional search space. NSGA-II is used for multi-objective optimization, with population size 150, crossover probability 0.9, mutation probability 0.15, and maximum number of generations 300. Total optimization runtime is 6.5 hours on a 32 core workstation. The average runtime of a single CFD simulation on the 32-core workstation is 47 minutes, including mesh generation, steady-state solution, and post-processing. One forward prediction of the radial basis function surrogate model takes 0.3 seconds, enabling a total of 45,000 surrogate model calls over 300 generations with 150 individuals per generation, avoiding an equivalent total of approximately 35,250 hours of CFD computation. Convergence is monitored using the hypervolume ratio. The hypervolume ratio starts at 0.32 in the first generation, rises to 0.78 by generation 100, reaches 0.91 by generation 200, and after generation 250 the increment per generation falls below 0.002. The convergence criterion of a relative improvement in hypervolume ratio below 0.5% over ten consecutive generations is satisfied at generation 276. At the end of the optimization, the number of non-dominated solutions on the Pareto front is 23, representing 15.3% of the total population in the final generation.

At each iteration, solutions individually and automatically call a generic performance evaluation module to measure three quantities, which are then aggregated into a 3D objective vector. The crowding distance operator is introduced to preserve the population diversity and avoid collapsing solutions into a local region while the algorithm ranks individuals based on non-dominance criteria. The criterion for convergence adopts the hypervolume ratio to track the variation in "the coverage of generation differences". Convergence is stated as when less than 0.5% of improvement over ten successive generations is observed, and the final Pareto optimal solution set is output.

None of the solutions can be improved further on one performance measure without making it worse on another, so this set of solutions is called a Pareto optimal boundary. The mathematical expression is as follows:

$$P=\{\mathbf{x}\in X \mid \exists \mathbf{x}'\in X: f_i(\mathbf{x}')\leq f_i(\mathbf{x})\ \forall i, \text{ and } f_j(\mathbf{x}')<f_j(\mathbf{x}) \text{ for some } j\} \quad (7)$$

P represents the Pareto front set; X is the feasible design domain; $f_i(\mathbf{x})$ is the function value of the i-th objective, corresponding to ecological disturbance f_1, power generation efficiency f_2, and visual harmony f_3, respectively; x represents a candidate design scheme. This set intuitively presents the trade-offs among the three, supporting decision-makers in identifying the candidate scheme with the most comprehensive benefits.

2.4.2. Scheme selection and BIM-driven refinement

Selection of a compromise solution along the Pareto front must take into account considerations of technical feasibility and priority of implementation. The Ideal Point Method is employed for the trade-offs, where the ideal values for each objective are the minimum ecological disturbance, the maximum power generation, and the maximum aesthetic value, respectively. The Euclidean distance to the ideal point is computed from each solution as follows:

$$d_k=\sqrt{\sum_{i=1}^{3}\left(\frac{f_i^k-f_i^{\text{ideal}}}{\Delta f_i}\right)^2} \quad (8)$$

d_k is the distance from the k-th Pareto solution to the ideal point; f_i^k is its i-th objective value; f_i^{ideal} is the theoretical optimal value of the objective; Δf_i is the actual range of values for this dimension, used for normalization. The solution with the smallest distance is selected as the recommended solution, ensuring a globally optimal approximation across the three dimensions.

The chosen solution is then brought into a building information modeling (BIM) environment for multidisciplinary, detailed design collaboration. Using Revit, a composite model of structural foundations, electrical wiring, landscape connections, and maintenance paths is created. Every element has material properties, construction processes, and lifecycle information. The chosen solution is then brought into a BIM environment using Revit, where structural foundations, electrical wiring, landscape connections, and maintenance paths are modeled with associated material and lifecycle properties. The model outputs to IFC standard format, allowing for clash detection, quantity take-off, and schedule simulation by the construction team.

3. Multi-dimensional Integration Performance Verification of Coastal Wind Energy Layout Scheme

3.1. Experimental Data

The study area is a representative open coastal plain in a temperate zone, extending approximately 4.2 km in an east-west direction and encompassing three ecological subsystems: sand dunes, salt marshes, and intertidal flats. Monitoring and simulation cover one full annual cycle from January to December. The ecological observation system comprises eight automatic weather stations, three X-band bird radars, and four UAV aerial surveys per year. A total of 120 participants completes the VR evaluation, recruits through stratified sampling to reflect age, length of residence, and occupational background. CFD simulations are executed in ANSYS Fluent using RANS k-ε turbulence closure, and the VR evaluation environment is developed in Unity. The mean annual wind velocity is 6.8 m/s, and the main wind direction is SE-ENE. A prototype array of 32 turbines is installed for testing; each turbine has a rated power of 15 kW, with adjustable tower height and blade tilt angle. Each turbine uses a rotor diameter of 18 m and cut in wind speed of 3 m per second with rated speed of 11 m per second. The mean annual wind velocity is 6.8 m/s, and the main wind direction is SE-ENE.Each turbine has a rotor diameter of 18 m, a cut-in wind speed of 3 m/s, and a rated wind speed of 11 m/s. Tower height is adjustable between 20 m and 60 m in 5 m increments, and blade tilt angle is adjustable between 0° and 30°. Both horizontal-axis and vertical-axis rotor configurations are included in the design library, selected on the basis of start-up wind speed, rated operating conditions, and noise radiation pattern. The inter-turbine spacing variable ranges from 3 to 8 rotor diameters, and surface material reflectivity is parameterized from 0.2 to 0.7 to cover the range of PBR rendering inputs used in VR evaluation. CFD simulations are executed in ANSYS Fluent using RANS k-ε turbulence closure, with a computational domain radius of 2 km and approximately 2.8 million unstructured tetrahedral cells. The NSGA-II optimizer uses a population size of 150, crossover probability of 0.9, mutation probability of 0.15, and a maximum of 300 generations, running on a 32-core workstation. The DEM is created from LiDAR (light detection and ranging) point clouds with a spatial resolution of 0.5 m. Vegetation type is used to assign surface roughness. All the compared schemes are executed under the same computational setting, initial conditions, and boundary conditions. Mesh independence verification is also conducted for the CFD mesh to guarantee consistency in the Results. Standalone, the data acquisition, processing, and optimization are automated using custom scripts and analyses, minimizing the human-induced biases.

3.2. Wind Turbine Morphology-Performance Coupled Response Evaluation

A parametric grid covering 20–60 m and 0°–30° is constructed using tower height and blade tilt angle as input variables. Each combination is input to a CFD-calibrated radial basis function surrogate model, outputting normalized annual power generation and wake extension radius. A scalarized weighted strategy is used to fuse the two objectives, with weights set according to the aerodynamic efficiency priority principle. A global minimum search is used to locate the optimal solution for overall performance, and locally optimal tilt angles are extracted column-by-column along the height dimension to form a Pareto approximate trajectory. All data points strictly correspond to the physical simulation response, without interpolation or extrapolation.

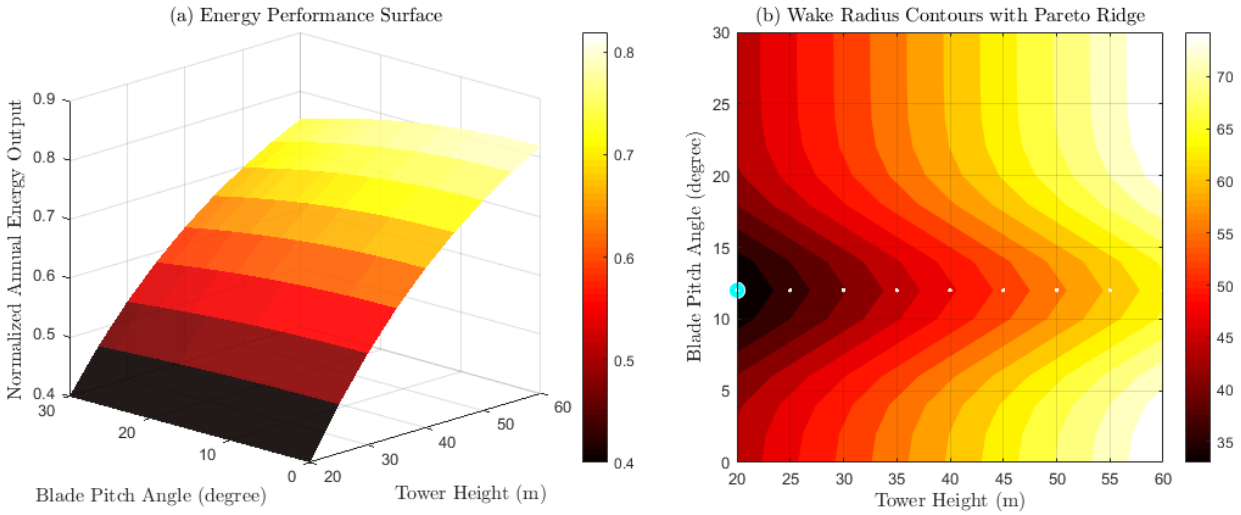

Fig. 4. Coupled response of tower height and blade tilt angle to normalized annual power generation and wake radius in meters.

Fig. 4 reveals the coupled control mechanism of tower height and blade tilt angle on wind energy capture efficiency and wake influence. Fig. 4(a) is the three-dimensional response surface of normalized annual power generation, with tower height ranging from 20 to 60 m and blade tilt angles from 0° to 30°. The vertical axis represents normalized power generation (range 0.4–0.9). Data shows that power generation increases with tower height, but the growth rate decreases; and excessive tilt angles lead to a decrease in power generation and aerodynamic efficiency. Fig. 4(b) is a contour plot of the

wake extension radius (unit: meters), with the same horizontal and vertical axis definitions, and color gradients reflecting the wake scale. The wake radius shows an increasing trend with the tower, originating from the enhanced wind shear at higher altitudes. A local minimum is observed at an inclination angle of approximately 12°, indicating that the blades exert the weakest airflow disturbance at this angle. The dots and trajectory indicate the Pareto optimal solution band—that is, maintaining high power generation while keeping the wake at a low level. This result shows that simply pursuing maximum power generation can significantly amplify the wake's impact, while synergistic optimization can achieve a balance between performance and disturbance at an inclination angle of around 12°.

3.3. Aesthetic Acceptance Assessment of Wind Energy Facilities under Demographic Dimensions

A sample of 120 subjects is formed, stratified by age and length of residence. A virtual reality system is employed to obtain aesthetic responses of Participants to wind energy facilities in a simulated coastal setting. Subjective esthetic evaluation in four esthetic dimensions is recorded by using a 7-point Likert scale. During data pre-processing, a mixed-effects model is employed to account for the individual variability and compute the mean score for each demographic group. Subsequently, both age and length of residence are categorized into four gradients and four levels within a matrix following a 4x4 evaluation style. A repeated measurement design is utilized to guarantee the stability of the data.

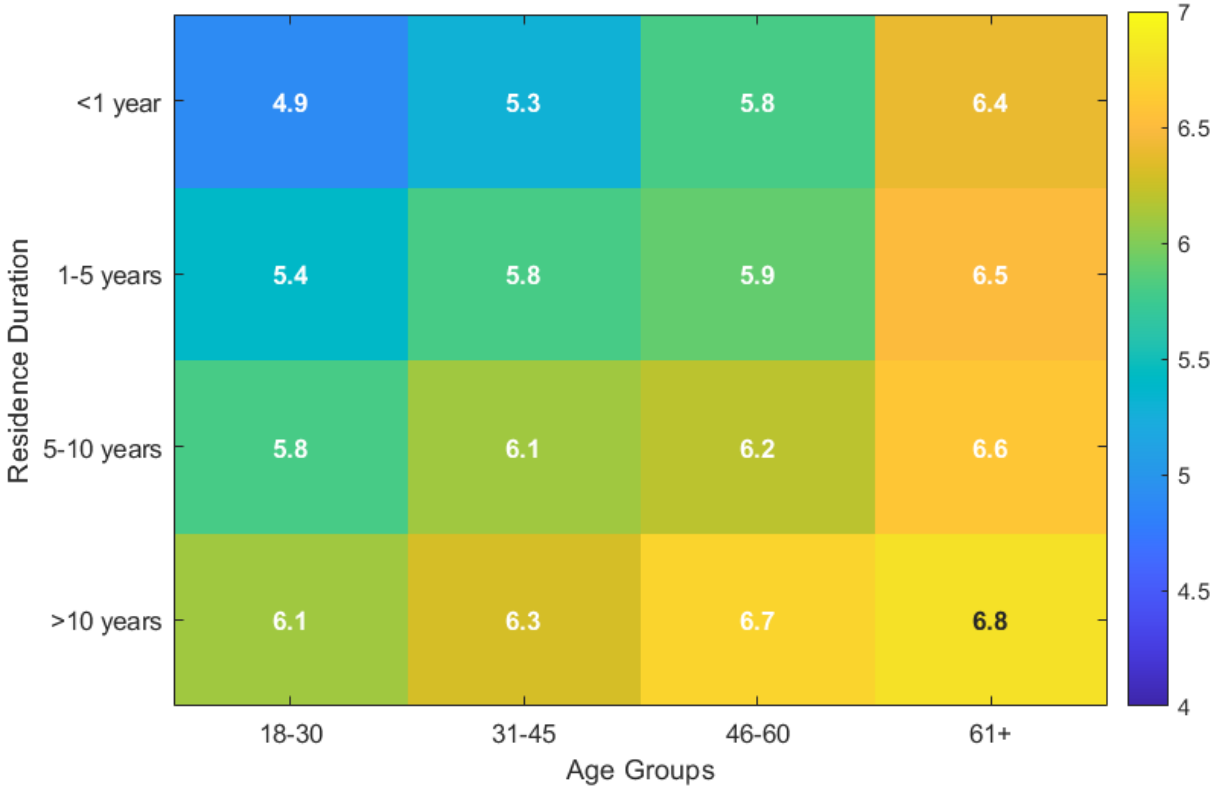

Fig. 5. VR aesthetic acceptance scores across age groups and residence duration based on 7 point rating scale.

Fig. 5 shows systematic demographic differences in aesthetic scores across the age-by-residence-duration matrix. The x-axis represents age group, the y-axis represents length of residence within each age group, and cell color reflects the mean score on the 7-point Likert scale. The data matrix indicates that the aesthetic acceptance of wind energy facilities by the public increases with age, with the oldest age group (61 and above) awarding the highest scores (6.4-6.8). The length of residence factor reveals a more prominent effect, as local (residing for more than 10 years) residents tend to agree more than temporary ones. This pattern of distribution implies that environmental familiarity plays a key role in shaping visual preference—prolonged coastal exposure may enable residents to better accept artificial structures. The 18–30-year-old short-term-resident group gives the lowest score (4.9), indicating that the younger migrant population has a higher bar when it comes to landscape authenticity. The interaction between age and residency duration points to the socially constructed nature of aesthetic judgment; residency experience gradually reconstructs an individual's acceptance threshold for the integration of technological facilities into the natural landscape through accumulated environmental cognition.

3.4. Comparison of Ecological Disturbance Control Capabilities

Under the two indicators of vegetation restoration cycle and bird avoidance rate, the proposed scheme is compared with four other methods: regular grid, random layout, wind speed maximization, and landscape sight avoidance, to quantify the ecological disturbance control capabilities. The vegetation restoration cycle refers to the number of months required for native vegetation cover to recover to 90% after

construction; the bird avoidance rate is calculated based on radar monitoring data, representing the proportion of migratory bird flocks deviating from their original paths during wind turbine operation. This indicator reflects behavioral detour rather than mortality risk and indicates spatial compatibility of the layout. The bird avoidance rate directly measures the degree to which operating wind turbines alter the spatial behavior of migrating birds. A high avoidance rate implies that birds actively change flight paths to bypass the wind farm area, leading to additional energy expenditure, extended migration time, and potential compression of habitat connectivity. An avoidance rate below 60% indicates that most flocks still attempt to cross the wind farm, increasing the risk of collision with rotating blades. The avoidance rates recorded in this study range from 74.1% to 92.3% during the migration season, demonstrating that the layout successfully diverts bird flight trajectories away from core activity zones and thereby maintains corridor continuity. This indicator together with the vegetation recovery cycle forms two complementary dimensions of ecological disturbance assessment: the vegetation recovery cycle reflects surface disruption during the construction phase, while the bird avoidance rate reflects ongoing disturbance to animal behavior during the operational phase. Vegetation recovery is tracked using monthly NDVI change derived from satellite images and field sampling records. Bird avoidance is derived from trajectory deviation statistics of radar tracks before and after turbine operation.

Comparisons are made under different seasons (breeding season/migratory season/inactive season).

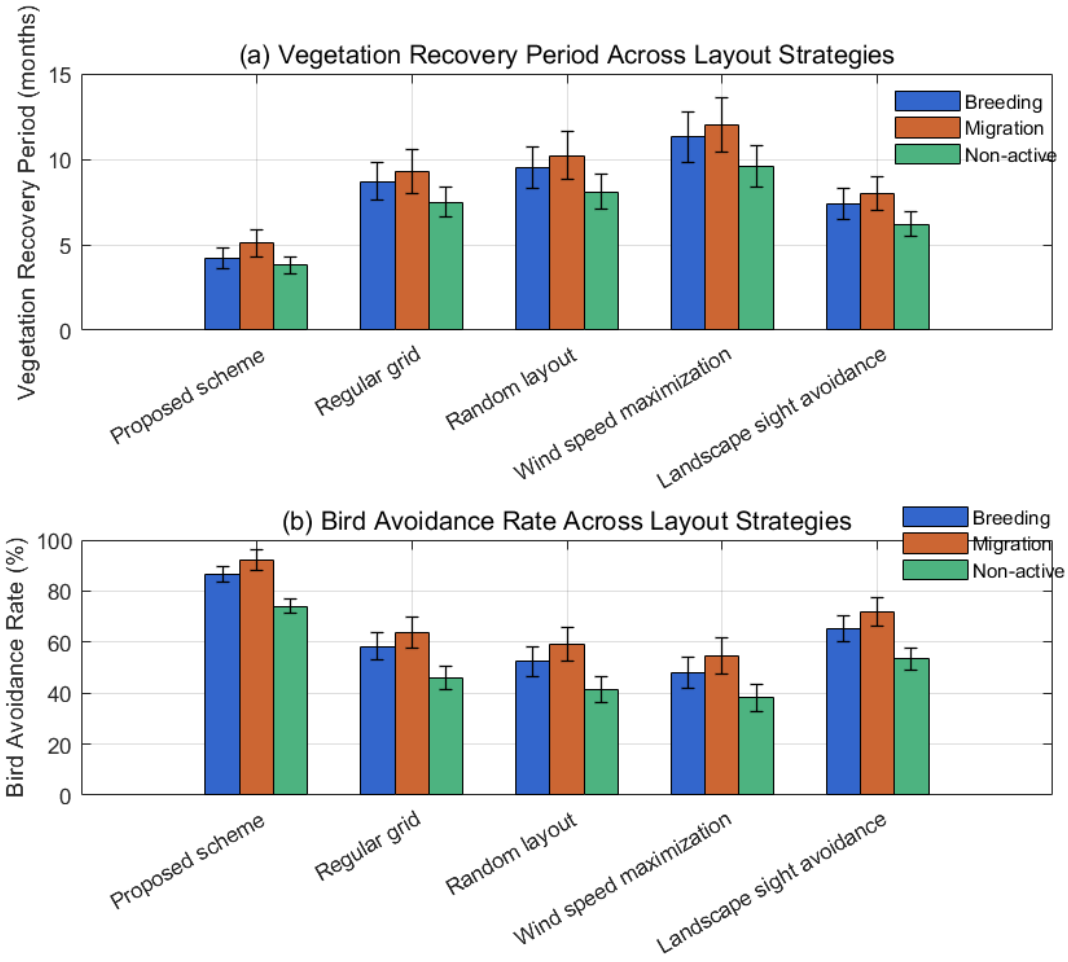

Fig. 6. Vegetation recovery cycle and bird avoidance rate across five layout strategies under breeding, migratory, and inactive seasons.

Fig. 6 depicts the disturbance response of different layout strategies to coastal ecosystems. The vegetation restoration cycle is directly affected by construction footprint and the degree of intrusion into sensitive areas: the scheme presented in this paper, due to its strict adherence to dynamic ecological sensitivity field constraints, exhibits minimal disturbance and the fastest recovery, with an average duration of 3.8 to 5.1 months. In contrast, wind speed maximization layouts often place wind turbines in high-energy areas such as dune ridges, exacerbating surface disturbance and prolonging vegetation rebuilding time. Bird avoidance rates are closely related to the intensity of the disruption of migration corridors by the spatial arrangement. The scheme presented in this paper, by integrating radar tracking data to actively avoid core flight paths, achieves a significantly higher avoidance rate during the migration season, with an average bird avoidance rate of

74.1%–92.3%. In contrast, regular grid and random layouts lack ecological path awareness, creating a physical barrier effect that forces bird flocks to passively detour or traverse risk areas. Seasonal differences further reveal the temporal sensitivity of ecological processes—habitat stability requirements are higher during the breeding season, while disturbance tolerance is relatively increased during the inactive season. Overall, only when the layout logic incorporates ecological dynamic mechanisms can low-disturbance performance be maintained across multiple seasonal phases.

3.5. Wind Energy Utilization Efficiency Stability Assessment

Wind gust influence is evaluated using hourly wind variance derived from meteorological tower measurements to examine layout stability under fluctuating wind conditions. A horizontal comparison is made with the four methods mentioned above using two indicators: the annual average power generation fluctuation coefficient and the wake disturbance index. The annual average power generation fluctuation coefficient is the ratio of the monthly power generation standard deviation to the mean; monthly generation data are derived from hourly simulation outputs aggregated into monthly totals and then normalized across the annual cycle. The wake disturbance index is calculated by weighted averaging of the downstream turbine inlet wind speed attenuation rate, wind speed attenuation is obtained from CFD sampling planes located two rotor diameters downstream of each turbine. Reflecting the degree of disturbance of the layout to the overall wind field. Comparisons are made under different shoreline slopes (gentle type <3°, medium type 3–8°, steep type >8°).

Table 2. Wind gust response comparison

Layout	Gust response index
Proposed scheme	0.21
Regular grid	0.34
Random layout	0.39
Wind speed maximization	0.31
Landscape sight avoidance	0.27

Note:Gust response index for each layout strategy, computed as the ratio of peak instantaneous wind speed deviation to mean annual speed, averaged across all turbine positions

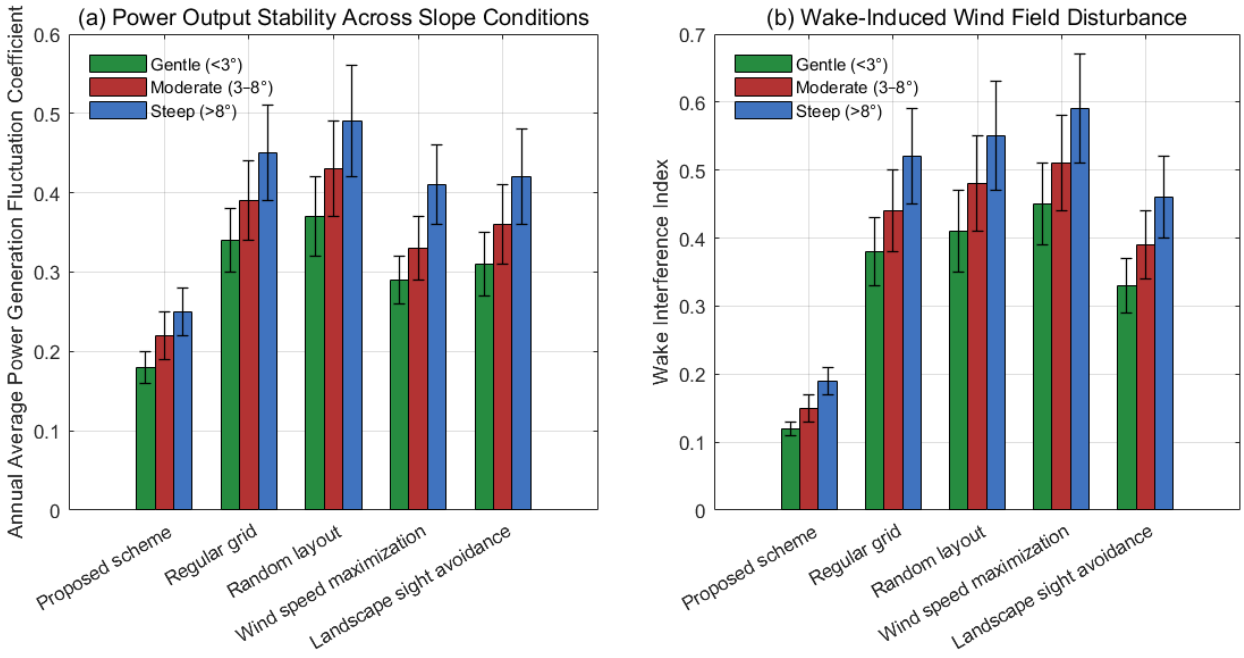

Fig. 7. Annual power fluctuation coefficient and wake disturbance index under different shoreline slopes.

Fig. 7 presents the energy output fluctuation and wind field disturbance control among the different arrangement strategies. The presented approach keeps both the annual power generation variation coefficient (average 0.18-0.25) and the wake disturbance index (average 0.12-0.19) low under a wide range of shoreline slopes. It comes from the morphologic parameters dynamically coupled with the local wind environment, which act as a buffer to sudden changes of

wind speed brought by sea and land winds and topographic disturbances. However, the densely packed formation exacerbates wake superposition and further amplifies the wake disturbance index on a steep slope for the wind speed maximization layout, pursuing strong wind energy acquisition. Both regular grid and random layouts do not have active control of the flow path through the wind farm, and, as a result, wake dissipation is slow, and downstream turbines are forced to work inefficiently for extended periods of time. The landscape visibility avoidance approach does eliminate visually sensitive areas, but does not integrate aerodynamic performance maximization, and thus is more variable than the proposed approach when considering different slopes. On gentle shorelines, due to higher airflow uniformity, all methods perform well; however, as the slope increases, the terrain acceleration effect and separation flow intensify, placing higher demands on the aerodynamic adaptability of the layout. This paper's proposed solution achieves terrain-responsive configuration of wind turbine tilt angle and height through generative adaptation, weakening wake intensity and smoothing power output, demonstrating the adaptability advantages of multi-objective collaboration to complex coastal wind fields.

3.6. Visual Fusion Measurement Analysis

Comparisons are conducted using two indicators: landscape visual entropy and public acceptance score. Landscape visual entropy is calculated based on the digital elevation model and wind turbine geometry to determine the complexity of the sightline profile; the entropy value is derived from skyline edge extraction and grayscale distribution of rendered VR views. The public acceptance score is obtained from the 7-point Likert scale VR ratings; for cross-scheme reporting consistency in Table 3, raw 7-point scores are linearly rescaled to a 5-point scale using the transformation: normalized score = raw score × 5 / 7, applied uniformly across all layout strategies and viewpoint types. All values reported in the Public Acceptance Score column of Table 3 are therefore on the 5-point normalized scale, and the range of 3.92–4.31 for the proposed scheme corresponds to original 7-point ratings of approximately 5.5–6.0. All methods are tested on the same population sample. Comparisons are made among different viewpoint types (coastal walkway, viewing platform, residential balcony).

Table 3. Public acceptance score (5-point scale, Mean ± 95% CI)

Layout Strategy	Viewpoint Type	Landscape Visual Entropy (Mean ± Std)	Public Acceptance Score normalized to 5 point scale (Mean ± 95% CI)
Proposed scheme	Coastal promenade	1.82 ± 0.14	4.31 ± 0.12
	Observation deck	2.05 ± 0.17	4.15 ± 0.14
	Residential balcony	2.38 ± 0.21	3.92 ± 0.16
Regular grid	Coastal promenade	3.47 ± 0.26	2.84 ± 0.18
	Observation deck	3.62 ± 0.28	2.67 ± 0.20
	Residential balcony	3.91 ± 0.31	2.41 ± 0.22
Random layout	Coastal promenade	3.85 ± 0.30	2.53 ± 0.19
	Observation deck	4.02 ± 0.33	2.36 ± 0.21
	Residential balcony	4.27 ± 0.35	2.18 ± 0.23
Wind speed maximization	Coastal promenade	3.21 ± 0.24	2.97 ± 0.17
	Observation deck	3.44 ± 0.27	2.78 ± 0.19
	Residential balcony	3.76 ± 0.30	2.52 ± 0.21
Landscape sight avoidance	Coastal promenade	2.64 ± 0.20	3.42 ± 0.15
	Observation deck	2.89 ± 0.23	3.21 ± 0.17
	Residential balcony	3.18 ± 0.25	2.95 ± 0.19

Note: Std stands for Standard Deviation, and CI stands for Confidence Interval

Table 3 shows that the differences in visual integration stem from the depth of coupling between morphological organization logic and environmental context. The proposed scheme, through dynamic ecological field constraints and aesthetic feedback loops, ensures that the wind turbine layout follows the dune orientation and the sea-line visual corridor, resulting in a smooth transition in the visual profile and significantly lower visual entropy than other strategies. The average landscape visual entropy is 1.82-2.38, and the average public acceptance is 3.92-4.31. Regular grids and random layouts ignore terrain guidance, creating mechanically repetitive or disorderly and abrupt skylines, leading to increased contour complexity. While the wind speed maximization scheme optimizes energy capture, it exacerbates

the sense of oppression in the foreground. Landscape visual avoidance only avoids static viewpoints, failing to coordinate multi-scale visual rhythms, resulting in a sense of separation at mid- to long-distance distances. Public acceptance response exhibits a spatial gradient: the coastal walkway has higher tolerance due to distance buffering; residents' balconies, as interfaces for daily life, show a sharp increase in sensitivity to scale and materials. The proposed solution maintained high scores across all three viewpoints because it transforms technical facilities into elements of landscape rhythm, rather than isolated structures. The simultaneous generation of visual order and functional logic allows infrastructure to be implicitly embedded at the perceptual level, rather than forcibly avoided.

3.7. Comparison of Spatial Adaptability and Layout Flexibility

The spatial adaptability and layout flexibility are quantified using two indicators: solution adjustment response time and terrain adaptation error. Solution adjustment response time refers to the computation time (seconds) required to generate a new feasible solution after adding an ecological restriction zone; terrain adaptation error is the root mean square deviation (meters) between the wind turbine foundation point and the actual terrain elevation. All methods are run on the same dataset. Comparisons are made under scenarios with newly added ecological restriction zones (area percentages of 5%, 10%, and 15%).

Table 4. Comparison of spatial adaptability and layout flexibility

Layout Strategy	Ecological Restricted Areas	Adjustment Response Time (s) (Mean ± SD)	Terrain Adaptation Error (m) (Mean ± SD)
Proposed scheme	5%	42.3 ± 3.1	0.18 ± 0.02
	10%	48.7 ± 3.8	0.19 ± 0.02
	15%	55.2 ± 4.2	0.20 ± 0.03
Regular grid	5%	186.4 ± 12.5	0.64 ± 0.08
	10%	210.9 ± 14.3	0.67 ± 0.09
	15%	235.6 ± 16.1	0.71 ± 0.10
Random layout	5%	28.5 ± 2.4	0.82 ± 0.11
	10%	31.2 ± 2.7	0.85 ± 0.12
	15%	34.8 ± 3.0	0.88 ± 0.13
Wind speed maximization	5%	152.7 ± 10.8	0.58 ± 0.07
	10%	178.3 ± 12.2	0.61 ± 0.08
	15%	203.9 ± 13.7	0.65 ± 0.09
Landscape sight avoidance	5%	124.6 ± 9.3	0.43 ± 0.05
	10%	142.1 ± 10.6	0.46 ± 0.06
	15%	161.8 ± 11.9	0.49 ± 0.07

Table 4 presents the response performance and terrain fit capabilities of the five layout strategies under dynamic constraint perturbations. The proposed scheme maintains high reconstruction efficiency even after the addition of ecological restriction zones, with an average adjustment response time of no more than 55.2s and a terrain fit error of no more than 0.20m. This is far superior to regular grid or wind speed maximization methods that rely on global re-optimization, attributed to the locally adjustable parameterization logic and lightweight proxy model embedded in the generative framework, avoiding system-wide rollback. Although the random layout is computationally fast, its unconstrained initial distribution makes large elevation jumps at the anchors and leads to a terrain fitting error of nearly 0.9m in foundation points, which is not qualified for the accuracy requirement in offshore soft soil foundation construction. Instead, the approach presented in this paper constrains the location of wind turbine foundations by modeling ecological sensitivity as a field in combination with terrain curvature, demonstrating that stable micro-topographic units permit precise locations. The landscape sightline avoidance approach does maximize the visual dimension, but it does not account for terrain feedback, resulting in a fit error of more than 0.4 meters. With the increasing size of restricted regions, the response time of all methods tends to increase. Nonetheless, the proposed scheme is smaller, capturing the merits of topological flexibility and an incremental update mechanism, which makes it applicable to the case where ecological boundaries change frequently, such as in a coastal region.

4. Conclusion

The collaborative design system built in this work combines dynamic ecological perception, aerodynamic performance simulation, and immersive public feedback with a unified generating logic, which underpins the dynamic ecological perception technology that reduces the isolated targeting and delayed response observed in conventional wind energy layout design. Instead of the static protection zoning, the ecologically sensitive field is presented in a spatiotemporally continuous way, allowing design constraints to attune to environmental rhythms. The reduced-order wind field surrogate model is coupled with morphological variables to simultaneously optimize the energy-harvesting efficiency and the control of the airflow disturbances. VR-based aesthetic scoring is converted into computable weights, providing a quantitative direction for visual integration. Instead of the extremum of one indicator, the multi-objective optimization procedure condenses a Nash solution among ecological minimization, performance robustness, and landscape harmonization. This study presents performance advantages within the tested scenarios. The general strategy moves beyond the rigid 'embed' and 'avoid' lines of thought (instead embracing their dialectical wavering), towards a coevolution of technological systems and coastal environment, offering a data-informed, perception-closed-loop, and morphologically-malleable path reference for infrastructure design in extremely sensitive contexts. Several limitations warrant acknowledgment. The radial basis function surrogate model is trained on 200 CFD configuration samples from a single temperate-zone coastal plain, and its generalization accuracy may decrease in coastal environments with substantially different terrain complexity, dominant wind directions, or tidal regime. The VR evaluation sample of 120 participants is drawn from one geographic region, limiting the demographic representativeness of the derived aesthetic weights for populations with different landscape exposure histories. The bird avoidance metric captures behavioral detour rates under operational turbine conditions but does not account for cumulative mortality risk or multi-year population-level effects, which would require longer-term field monitoring beyond the one-year observation window of this study.

Acknowledgement

N/A

Authorship Contribution Statement

Shilong Xu: Writing-Original draft preparation, Conceptualization, Supervision, Project administration.

Guangyu Yang: Methodology, Software, Validation.

Conflicts of Interest

The authors declare that there is no conflict of interest regarding the publication of this paper.

References

[1] A. M. AlQahtani, "A comprehensive assessment of wind energy potential and wind farm design in a coastal industrial city," World Journal of Engineering, vol. 22, no. 3, pp. 529-539, 2025.

[2] L. Chen, Y. Hu, R. Wang, X. Li, Z. Chen, J. Hua, A. I. Osman, M. Farghali, L. Huang, J. Li, L. Dong, D. W. Rooney, and P.-S. Yap, "Green building practices to integrate renewable energy in the construction sector: a review," Environmental Chemistry Letters, vol. 22, no. 2, pp. 751-784, 2024.

[3] M. S. Genç, F. Karipoğlu, K. Koca, and Ş. T. Azgın, "Suitable site selection for offshore wind farms in Turkey's seas: GIS-MCDM based approach," Earth Science & Informatics, vol. 14, no. 3, pp. 1213-1225, 2021.

[4] M. Parhamfar, I. Sadeghkhani, and A. M. Adeli, "Towards the application of renewable energy technologies in green ports: technical and economic perspectives," IET Renewable Power Generation, vol. 17, no. 12, pp. 3120-3132, 2023.

[5] F. Al Mubarak, R. Rezaee, and D. A. Wood, "Economic, societal, and environmental impacts of available energy sources: a review," Eng, vol. 5, no. 3, pp. 1232-1265, 2024.

[6] V. Perricone, M. Mutalipassi, A. Mele, M. Buono, D. Vicinanza, and P. Contestabile, "Nature-based and bioinspired solutions for coastal protection: an overview among key ecosystems and a promising pathway for new functional and sustainable designs," ICES Journal of Marine Science, vol. 80, no. 5, pp. 1218-1239, 2023.

[7] A. O. Adekanmbi, N. Ninduwezuor-Ehiobu, A. Abatan, U. Izuka, E. C. Ani, and A. Obaigbena, "Implementing health and safety standards in offshore wind farms," World Journal of Advanced Research and Reviews, vol. 21, no. 2, pp. 1136-1148, 2024.

[8] A. P. Crowle and P. R. Thies, "Floating offshore wind turbines port requirements for construction," Proceedings of the Institution of Mechanical Engineers, Part M: Journal of Engineering for the Maritime Environment, vol. 236, no. 4, pp. 1047-1056, 2022.

[9] C. Maienza, A. M. Avossa, V. Picozzi, and F. Ricciardelli, "Feasibility analysis for floating offshore wind energy," The International Journal of Life Cycle Assessment, vol. 27, no. 6, pp. 796-812, 2022.

[10] O. Khalid, G. Hao, C. Desmond, H. Macdonald, F. D. McAuliffe, G. Dooly, and W. Hu, "Applications of robotics in floating offshore wind farm operations and maintenance: literature review and trends," Wind Energy, vol. 25, no. 11, pp. 1880-1899, 2022.

[11] M. Jahangiri, F. Karimi Shahmarvandi, and R. Alayi, "Renewable energy-based systems on a residential scale in southern coastal areas of Iran: trigeneration of heat, power, and hydrogen," Journal of Renewable Energy and Environment, vol. 8, no. 4, pp. 67-76, 2021.

[12] R. Zahedi, E. Sadeghitabar, and A. Ahmadi, "Solar energy potential assessment for electricity generation in the southeastern coast of Iran," Future Energy, vol. 2, no. 1, pp. 15-22, 2023.

[13] J. Buyse, K. Hostens, S. Degraer, and A. De Backer, "Offshore wind farms affect the spatial distribution pattern of plaice Pleuronectes platessa at both the turbine and wind farm scale," ICES Journal of Marine Science, vol. 79, no. 6, pp. 1777-1786, 2022.

[14] B. Yang, B. Liu, H. Zhou, J. Wang, W. Yao, S. Wu, H. Shu, and Y. Ren, "A critical survey of technologies of large offshore wind farm integration: summary, advances, and perspectives," Protection and Control of Modern Power Systems, vol. 7, no. 2, pp. 1-3, 2022.

[15] P. Beiter, J. T. Rand, J. Seel, E. Lantz, P. Gilman, and R. Wiser, "Expert perspectives on the wind plant of the future," Wind Energy, vol. 25, no. 8, pp. 1363-1378, 2022.

[16] Q. V. Dinh, H. Mosadeghi, P. H. T. Pereira, and P. G. Leahy, "A geospatial method for estimating the levelised cost of hydrogen production from offshore wind," International Journal of Hydrogen Energy, vol. 48, no. 40, pp. 15000-15013, 2023.

[17] C. Li, J. M. Mogollón, A. Tukker, and B. Steubing, "Environmental impacts of global offshore wind energy development until 2040," Environmental Science & Technology, vol. 56, no. 16, pp. 11567-11577, 2022.

[18] A. M. Scheld, J. Beckensteiner, D. M. Munroe, E. N. Powell, S. Borsetti, E. E. Hofmann, and J. M. Klinck, "The Atlantic surfclam fishery and offshore wind energy development: 2. assessing economic impacts," ICES Journal of Marine Science, vol. 79, no. 6, pp. 1801-1814, 2022.

[19] H. Patidar, V. Shende, P. Baredar, and A. Soni, "Comparative study of offshore wind energy potential assessment using different Weibull parameters estimation methods," Environmental Science and Pollution Research, vol. 29, no. 30, pp. 46341-46356, 2022.

[20] T. Egeland-Eriksen, J. F. Jensen, Ø. Ulleberg, and S. Sartori, "Simulating offshore hydrogen production via PEM electrolysis using real power production data from a 2.3 MW floating offshore wind turbine," International Journal of Hydrogen Energy, vol. 48, no. 74, pp. 28712-28732, 2023.

[21] S. S. H. Dehshiri and S. J. H. Dehshiri, "Locating wind farm for power and hydrogen production based on geographic information system and multi-criteria decision making method: an application," International Journal of Hydrogen Energy, vol. 47, no. 58, pp. 24569-24583, 2022.

[22] M. M. Bertsiou, A. P. Theochari, and E. Baltas, "Multi-criteria analysis and geographic information systems methods for wind turbine siting in a North Aegean island," Energy Science & Engineering, vol. 9, no. 1, pp. 4-18, 2021.

[23] M. Min, M. Brazell, A. Tomboulides, M. Churchfield, P. Fischer, and M. Sprague, "Towards exascale for wind energy simulations," The International Journal of High Performance Computing Applications, vol. 38, no. 4, pp. 337-355, 2024.

[24] S. E. Haupt, B. Kosović, L. K. Berg, C. M. Kaul, M. Churchfield, J. Mirocha, D. Allaerts, T. Brummet, S. Davis, A. DeCastro, S. Dettling, C. Draxl, D. J. Gagne, P. Hawbecker, P. Jha, T. Juliano, W. Lassman, E. Quon, R. K. Rai, M. Robinson, W. Shaw, and R. Thedin, "Lessons learned in coupling atmospheric models across scales for onshore and offshore wind energy," Wind Energy Science, vol. 8, no. 8, pp. 1251-1275, 2023.

[25] S. Darabi, S. M. Monavari, S. A. Jozi, R. Rahimi, and A. Vafaeinejad, "Visual impact assessment of renewable energy developments with the application of multi-criteria decision-making method," Environment, Development and Sustainability, vol. 25, no. 5, pp. 4437-4451, 2023.

[26] S. E. Hosseini, O. Karimi, and M. A. AsemanBakhsh, "Experimental investigation and multi-objective optimization of savonius wind turbine based on modified non-dominated sorting genetic algorithm-II," Wind Engineering, vol. 48, no. 3, pp. 446-467, 2024.

[27] R. Alayi, M. Jahangiri, J. W. G. Guerrero, R. Akhmadeev, R. A. Shichiyakh, and S. A. Zanghaneh, "Modelling and reviewing the reliability and multi-objective optimization of wind-turbine system and photovoltaic panel with intelligent algorithms," Clean Energy, vol. 5, no. 4, pp. 713-730, 2021.

[28] B. Deng, X. Xu, M. Li, T. Ji, and Q. H. Wu, "Two-stage multi-objective optimization and decision-making method for integrated energy system under wind generation disturbances," CSEE Journal of Power and Energy Systems, vol. 10, no. 6, pp. 2564-2576, 2024.

[29] P. Tian, H. Chao, M. Rhudy, J. Gross, and H. Wu, "Wind sensing and estimation using small fixed-wing unmanned aerial vehicles: a survey," Journal of Aerospace Information Systems, vol. 18, no. 3, pp. 132-143, 2021.

[30] S. Courbis, K. Williams, J. Stepanuk, H. Etter, M. McManus, F. Campoblanco, and A. Pacini, "Technology gaps for monitoring birds and marine mammals at offshore wind facilities," Marine Technology Society Journal, vol. 58, no. 3, pp. 5-22, 2024.

[31] L. Liu and Y. Liang, "Wind power forecast optimization by integration of CFD and Kalman filtering," Energy Sources, Part A: Recovery, Utilization, and Environmental Effects, vol. 43, no. 15, pp. 1880-1896, 2021.

[32] A. Croce, S. Cacciola, M. Montero Montenegro, S. Stipa, and R. Pratico, "A CFD-based analysis of dynamic induction techniques for wind farm control applications," Wind Energy, vol. 26, no. 3, pp. 325-343, 2023.

[33] X. Dong, Z. Mao, Y. Sun, and X. Xu, "Short-term wind power scenario generation based on conditional latent diffusion models," IEEE Transactions on Sustainable Energy, vol. 15, no. 2, pp. 1074-1085, 2023.

[34] R. Pandit, D. Infield, and M. Santos, "Accounting for environmental conditions in data-driven wind turbine power models," IEEE Transactions on Sustainable Energy, vol. 14, no. 1, pp. 168-177, 2022.

[35] I. F. Martinez-Neri, "Supply chain integration in project manufacturing environments: the case of the offshore wind energy construction sector," International Journal of Energy Sector Management, vol. 19, no. 4, pp. 1075-1093, 2025.